Precipitation Simulation and Dynamic Response of a Transmission Line Subject to Wind-Driven Rain during Super Typhoon Lekima

Jianping Sun , Mingfeng Huang * , Sunce Liao , Wenjuan Lou

Posted Date: 16 April 2024

doi: 10.20944/preprints202404.0999.v1

Keywords: Transmission line; Wind-driven rain; Multiphase CFD simulation; Multi-scale simulation

 doi:10.20944/preprints202404.0999.v1

Article

Precipitation Simulation and Dynamic Response of a Transmission Line Subject to Wind-Driven Rain during Super Typhoon Lekima

Jianping Sun, Mingfeng Huang *, Sunce Liao and Wenjuan Lou

School of Civil Engineering & Architecture, Zhejiang University, Hangzhou,310058, China; mfhuang@zju.edu.cn, sunjianping@zju.edu.cn, 11912067@zju.edu.cn, louwj@zju.edu.cn
* Correspondence: mfhuang@zju.edu.cn

Abstract: Typhoons bring great damages to transmission line systems located in coastal areas. Strong wind and extreme precipitation are the main sources of damaging effects. Transmission lines suffered from wind-driven rain exhibit more susceptibility to damage due to the coupled effect of wind and rain water. This paper presents an integrated numerical simulation framework based on mesoscale WRF model, multiphase CFD model and FEM model to analyze the motions of a transmission line subjected to coupled wind and rain loads during typhoon events. A full-scale transmission line in Zhoushan island is employed to demonstrate the effectiveness of the proposed framework by simulating typhoon evolution in terms of wind fields and rainfall, solving the coupled wind and rain fields around the conductor and predicting the dynamic responses of the transmission line during Super Typhoon Lekima (2019). The results show that the horizontal displacements of the transmission line under the joint actions of wind and rain increases approximately 17%~18% compared to those of wind loads only. It is important to consider the coupled effects of wind-driven rain on conductors in the design of transmission lines under typhoon conditions.

Keywords: transmission line; wind-driven rain; multiphase CFD simulation; multi-scale simulation

1. Introduction

Typhoon is one of the major natural disasters threatening China's southeast coasts, causing much damages on buildings and infrastructures, including transmission tower-line systems of the power grid. The transmission tower-line system is a typical wind-sensitive structure with the characteristics of high flexibility, long span, and strong geometric non-linearity [1]. In 2005, typhoon "Damrey" caused the collapse of the power system of Hainan [2]; During hurricane "Sandy" in 2012 and hurricane "Irene" in 2011, over 200 transmission towers failed [3]; In 2015, the super typhoon "Mujigae" damaged 80 towers, impacting thousands of transmission lines [4]. Anthropogenic climate change has already substantially increased the exposure to extreme climate impact events worldwide, and further global warming is projected to exacerbate the weather hazards as we already see today [5]. Huang [6] indicates that under the backdrop of anthropogenic warming, both the landfall intensity and precipitation of typhoons in the southeastern coastal areas of China are expected to increase. The risk of typhoon-induced disasters on Southeast China is also significantly elevated [6].

The structural damage to transmission tower-line systems during typhoon weather can be attributed to strong winds and heavy rainfall. Burgh and Harton [7], as well as Burgh et al. [8], proposed a model equation to investigate rain-wind induced vibrations in a simple oscillator. They discovered that variations in the detuning parameter can result in saddle-node and Hopf bifurcations. Deng and Yang conducted numerical simulations [9,10] to study the response of a tower-line system under windy conditions. An's research [11,12], based on numerical simulations, considered the combined effects of wind and rain. However, their study primarily focused on the structural failure

 doi:10.20944/preprints202404.0999.v1

of towers. Some researchers analyzed the windage yaw of insulator strings and wires due to wind and rain loads. Yan et al. [13] introduced a numerical model of a transmission line section to calculate the dynamic swing of the suspension insulator. Zhou [14] proposed a model with a derived stability criterion to analyze the significant swing of the overhead conductor under wind and rain conditions. Fu and Li [15,16] established a calculation method for wind and rain loads on transmission conductors and discussed the effects of wind and rain excitation. Their results indicate that rain loads relative to wind loads could reach up to 22%. Zhou et al. [17,18] developed a two-dimensional model to investigate rain-wind induced vibration in transmission lines and discussed the aerodynamic instability zone using the Lyapunov stability criterion.

With the rapid progress of high-performance computation technique, numerical weather prediction (NWP) becomes an effective method to analyze the wind-rain climates and meteorological variables [19]. Weather research and forecasting model (WRF) is one of the most widely used NWP system designed for atmospheric research and operational weather forecasting. It is a state-of-the-art modeling system that simulates the dynamics and physics of the atmosphere to generate detailed weather forecasts and conduct meteorological research. WRF has gained popularity due to its flexibility, scalability, and ability to simulate a wide range of meteorological phenomena. The Advanced Research WRF (ARW) is one of the dynamical cores available within the WRF model based on a fully compressible set of atmospheric equations and is an appropriate model for simulating tropical cyclone systems. Many researchers have conducted typhoon related studies based on the ARW model and found that the ARW model could reproduce atmospheric conditions and agree well with the measurements during typhoons [20–24].

The coupled phenomena of wind and rain is referred to as wind-driven rain (WDR), that is, raindrops carried obliquely by strong winds. It occurs when raindrops get horizontal velocity component from wind blows, rather than falling straight down vertically. Wind-driven rain can lead to water intrusion, moisture damage, and potential issues like leaks, rot, or mold growth, affecting the thermal and moisture performance of buildings [25]. Researches have been carried out to study the WDR on building facades with full-scale measurements [26,27], semi-empirical methods [28,29], and numerical simulations. Although the numerical simulation of WDR with computational fluid dynamics (CFD) is complex and time-consuming, it can accurately determine the temporal and spatial distribution of WDR on complicated building facades, and the simulation accuracy has been validated with field measurements [30–34].

In this paper, a multiscale numerical framework is developed based on the WRF-CFD and FEM method to solve the WDR effects on the motion of a span of transmission lines located in Zhoushan island. Compared to existing researches, the presented method enables the prediction of the dynamic responses of transmission lines under real weather conditions based on multi-scale models coupling, and provides an insight into the wind-driven rain effect on conductors by means of multiphase CFD simulation. Section 2 proposes the methodology of the numerical simulation. Section 3 details the configurations of WRF model and presents the simulation results of Typhoon Lekima (2019). Section 4 presents the CFD simulation based on Eulerian Multiphase (EM) model of WDR flow field. Section 5 shows the finite element analysis of the transmission line under WDR condition. Section 6 provides discussion and conclusions.

2. Methods

Figure 1 demonstrates the workflow of the numerical simulation of WDR effects on a transmission line during a typhoon event. The framework consists of a mesoscale typhoon simulation through WRF, a CFD model of WDR multiphase flow and a finite element model of transmission line conductors.

 doi:10.20944/preprints202404.0999.v1

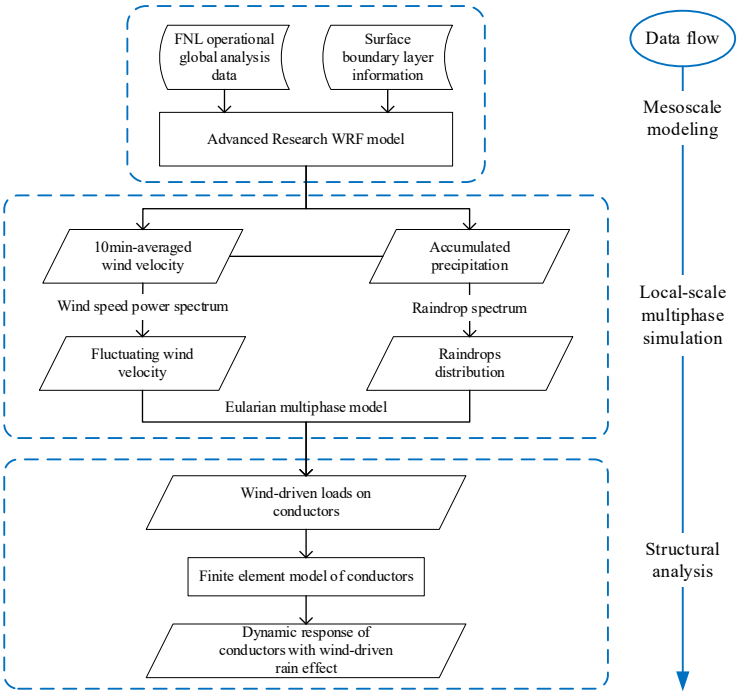

Figure 1. Flow chart of the numerical simulation of WDR effects on transmission lines.

2.1. Model Equations in WRF

The compressible, non-hydrostatic governing equations, i.e., time-averaged Reynolds equations, that govern the mesoscale NWP model are cast in flux forms and can be expressed in a terrain-following hydrostatic-pressure vertical coordinate as in literature [35,36]. Modelling of clouds microphysical process plays an important role in mesoscale convective storm simulations. The WRF Double-Moment 6-class (WDM6) microphysics scheme [37] is applied in this study. It is a bulk parameterization scheme that contains six water species: water vapor, cloud droplets, cloud ice, snow, rain, and graupel. Cloud particles are represented as particle size distribution (PSD) functions and are characterized by their moments in modelling of physical processes. The cloud-raindrop size distribution in WDM6 follows the normalized form given by [37],

$$n_X(D_X) = N_X \frac{\alpha_X}{\Gamma(\nu_X)} \lambda_X^{\alpha_X \nu_X} D_X^{\alpha_X \nu_X - 1} \exp[-(\lambda_X D_X)^{\alpha_X}], \tag{1}$$

$$\lambda_X = [\frac{\pi}{6} \rho_w \frac{\Gamma(\nu_X + 3/\alpha_X)}{\Gamma(\nu_X)} \frac{N_X}{\rho_a q_X}]^{1/3} \tag{2}$$

where $X = C, R$ refers to clouds or rain respectively; λ_X is the corresponding slope parameter, whereas ν_X and α_X are the two dispersion parameters.

The governing equation of the number concentration for each species is expressed as,

$$\frac{\partial N_X}{\partial t} = -\mathbf{V} \cdot \nabla_3 N_X - \frac{1}{\rho_a} \frac{\partial}{\partial z} (\rho_a N_X V_X) + S_X \tag{3}$$

where the first and second terms in the RHS represent the 3D advection and sedimentation for X, respectively. The term S_X represents the source and sink of number concentration for X.

The number-weighted-mean terminal velocity which is responsible for the sedimentation of the rain number concentration can be obtained by integrating the terminal velocity of rain water,

 doi:10.20944/preprints202404.0999.v1

$$\overline{V}_{NR}=\frac{\int V_R(D_R)dN_{DR}}{\int dN_{DR}}=\frac{a_R}{\lambda_R^{b_R}}\Gamma(2+b_R)(\frac{\rho_0}{\rho_a})^{1/2} \tag{4}$$

where $V_R(D_R)$ represents the terminal velocity of rain particles with diameter D_R. Based on Locatelli and Hobbs [38], the expression is given by,

$$V_R(D_R)=a_R D_R^{b_R}(\frac{\rho_0}{\rho_a})^{1/2} \tag{5}$$

2.2. WDR Simulation by Eulerian Multiphase Model

Under severe convective weather conditions, the coupled effect of strong wind and extreme rainfall will increase the load on transmission lines, and the rain water adhering to conductor surface can significantly change its aerodynamic characteristics. The WDR loads is related to the interaction of raindrops of different sizes with the wind flow. In the EM model, rain is regarded as various continuum and dilute phases with equivalent raindrop sizes, reducing the computation cost compared to Lagrangian Particle Tracking (LPT) model. Raindrops are divided into N groups according to the diameter D, and the kth rain phase represents the collection of raindrops of which the diameter $D\in\left[D_k-\Delta D/2, D_k+\Delta D/2\right]$, k=1, 2, …, N, where D_k is the kth diameter and $\Delta D=D_k-D_{k-1}$. The mass and momentum conservation equations for kth rain phase are presented as follows [30],

$$\frac{\partial\rho_{\mathrm{w}}\alpha_k}{\partial t}+\frac{\partial(\rho_{\mathrm{w}}\alpha_k u_{kj})}{\partial x_j}=0 \tag{6}$$

$$\frac{\partial\rho_{\mathrm{w}}\alpha_k u_{ki}}{\partial t}+\frac{\partial(\rho_{\mathrm{w}}\alpha_k u_{ki}u_{kj})}{\partial x_j}=\rho_{\mathrm{w}}\alpha_k g_i+\rho_{\mathrm{w}}\alpha_k\frac{3\mu C_{\mathrm{D}}Re_{\mathrm{R}}}{4\rho_{\mathrm{w}}D_k^{\,2}}\left(u_i-u_{ki}\right) \tag{7}$$

$$Re_{\mathrm{R}}=\frac{\rho_{\mathrm{a}}D_k}{\mu}\left|\boldsymbol{u}-\boldsymbol{u}_k\right| \tag{8}$$

where ρ_{w} and ρ_a are the density of water and air respectively; α_k is the volume fraction of the kth rain phase; $\boldsymbol{u}$ and $\boldsymbol{u}_k$ represent the velocity vector of wind and the kth rain phase respectively; g_i is the gravity along i direction; μ is the dynamic viscosity of air; C_{D} is the drag coefficient; Re_{R} represents the relative Reynolds number.

The second term on the RHS of Eq. (5) stands for the dragging of the wind flow. A raindrop in equilibrium state gives,

$$g_i+\frac{3\mu C_{\mathrm{D}}Re_{\mathrm{R}}}{4\rho_{\mathrm{w}}D_k^{\,2}}V_{\mathrm{t}}\left(D\right)=0, \tag{9}$$

where $V_{\mathrm{t}}\left(D\right)$ is the terminal velocity of raindrops with diameter D, and can be calculated by [38],

$$V_{\mathrm{t}}\left(D\right)=\begin{cases}0, & D\le 0.03\ \mathrm{mm};\\ 4.323\left(D-0.03\right), & 0.03\le D\le 0.6\ \mathrm{mm};,\\ 9.65-10.3\exp\left(-0.6D\right), & D\ge 0.6\ \mathrm{mm}\end{cases} \tag{10}$$

Then the drag coefficient C_{D} is constructed in the following form to hold Eq. (9),

Preprints.org (www.preprints.org) | NOT PEER-REVIEWED | Posted: 16 April 2024 doi:10.20944/preprints202404.0999.v1

$$C_{\mathrm{D}} = \frac{24}{Re_{\mathrm{R}}} \exp\left(-0.1FN + 0.201FN^2 - 0.03537FN^3 + 0.002537FN^4\right), \tag{11}$$

$$FN = \ln\left(1 + Re_{\mathrm{R}}\right). \tag{12}$$

2.3. Segment Model of Overhead Conductors under WDR Condition

The overhead conductor is hung with suspension insulator strings between transmission towers. A segment model of the conductor is depicted in Figure 2. In this model, the conductor segment is simplified as a cylinder, and α is the inclination of the segment; β is the wind angle towards the segment; U is the inflow wind velocity. The impact of WDR on conductor loads can be divided into two parts: the effect of raindrop impingement and the influence of rivulets on aerodynamic characteristic. According to Zhou [14], the wind-driven rain is sufficient to create upper and lower rivulets along the conductor while the lower rivulet is assumed to make little difference to the aerodynamic coefficients of the conductor and is neglected in this paper.

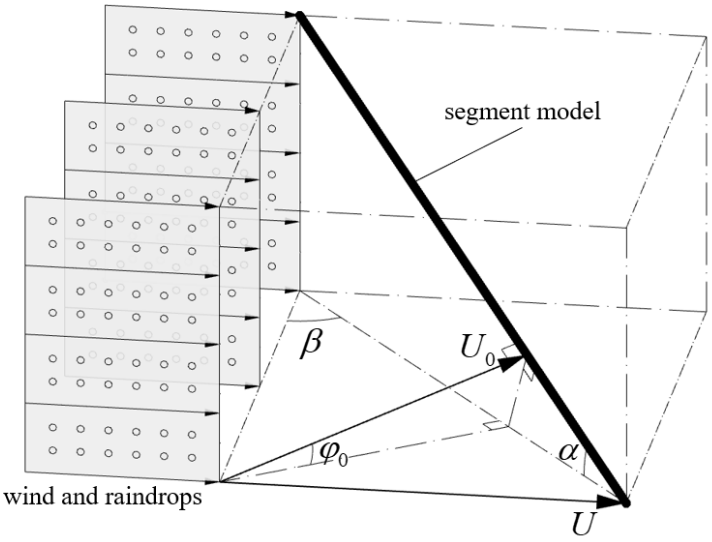

Figure 2. Segment model of a conductor.

Figure 3 shows the cross-section of the conductor. Under a certain rain-wind condition, upper rivulet occurs at the surface of the cylinder. Relative size of the height and the width to the diameter of the conductor are about 0.10 and 0.17 [17]. The balance angle of the upper rivulet is θ_0, determined by the coupled actions of gravity force, surface tension, and rain-wind loads. The unstable angle of the upper rivulet θ oscillates around θ_0 and the vibration of the rivulet can be considered harmonic [17,40]. Yet for simplicity, we assumed that the relative position of upper rivulet and conductor surface is fixed, that is, $\theta \equiv \theta_0$.

The component of the wind velocity U_0, perpendicular to the cylinder, can be expressed as,

$$U_0 = U\sqrt{1 - \cos^2\alpha \sin^2\beta}. \tag{13}$$

The initial attack angle is defined as,

$$\varphi_0 = \arctan(\sin\alpha \tan\beta). \tag{14}$$

The along-wind direction aerodynamic force per unit length of the cylinder can be expressed as,

 doi:10.20944/preprints202404.0999.v1

$$F(\lambda)=\frac{1}{2}\rho U_0^2 dC_F(\lambda), \tag{15}$$

where $C_F(\lambda)$ is the aerodynamic force coefficient and $\lambda=\theta+\varphi$; ρ is the air density; d is the diameter of the cylinder.

The aerodynamic force coefficient $C_F(\lambda)$ is derived as,

$$C_F(\lambda)=U_r^2(C_{drag}(\lambda)\cos\varphi-C_{lift}(\lambda)\sin\varphi)/U_0^2, \tag{16}$$

where C_{drag} and C_{lift} are the aerodynamic drag and lift force coefficients, respectively. U_r is the instantaneous relative wind velocity, and its horizontal and vertical component can be computed as,

$$U_{r,z}=U_0\cos\varphi_0-\dot{z}, \tag{17}$$

$$U_{r,y}=U_0\sin\varphi_0-\dot{y}, \tag{18}$$

where $\dot{z}$ and $\dot{y}$ are the horizontal and vertical velocity of the cylinder, respectively.

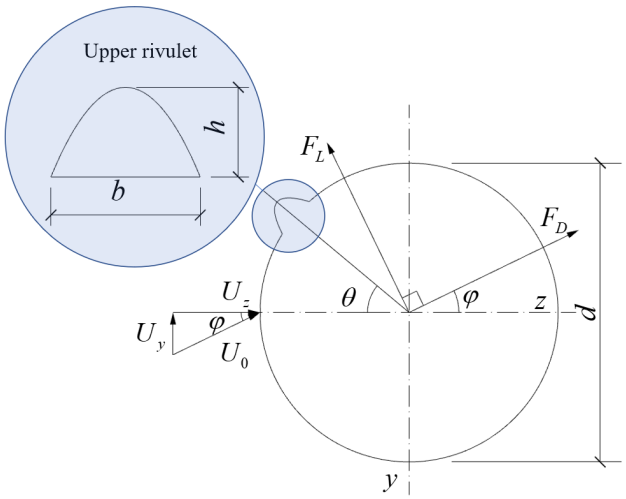

Figure 3. Cross-section of conductor model with upper rivulet.

3. Simulation of Typhoon Lekima

3.1. Overview of Lekima and WRF Model Settings

Super Typhoon Lekima in 2019, designated as No.1909, was a powerful and destructive tropical cyclone that struck East Asia in August 2019. It was the ninth named storm and the fourth typhoon of the 2019 Pacific typhoon season. Lekima originated from a tropical depression that formed east of the Northern Mariana Islands on July 30, 2019. The storm gradually intensified as it moved west-northwestward, reaching typhoon status on August 6. It continued to strengthen rapidly and became a super typhoon on August 7, with maximum sustained winds of 62 m/s. Lekima then made landfall in Wenling, Zhejiang province, China, on August 10. The impact of Typhoon Lekima was severe, causing widespread destruction and loss of life. It triggered torrential rainfall and strong winds, resulting in widespread flooding, landslides, and mudslides. The storm caused significant damage to infrastructure, including buildings, bridges and roads. It also disrupted transportation and led to power outages in several areas. According to the news report, Lekima has affected over 4 million people in Zhejiang Province. Crop damage has occurred on 103,000 hectares of land, with 13,000 hectares suffering complete crop loss. Additionally, over 14,000 houses have been damaged or collapsed due to the disaster, resulting in a direct economic loss of 7.44 billion yuan.

 doi:10.20944/preprints202404.0999.v1

As demonstrated in Figure 4, two-way nested static downscaling domains are used in WRF simulation and the simulation time period is from 0000 UTC 07 Aug to 0000 UTC 13 Aug in 2019. For the initial and boundary conditions of the outermost domain, 6-hourly Final Operational Global Analysis data of 1° resolution from the National Centers for Environmental Prediction (NCEP) are used, while the boundary conditions of the inner domains are provided by the domain above. The spatial and temporal resolutions of each domain are listed in Table 1. The schemes and parameterizations of physical processes of the simulation are listed in Table 2.

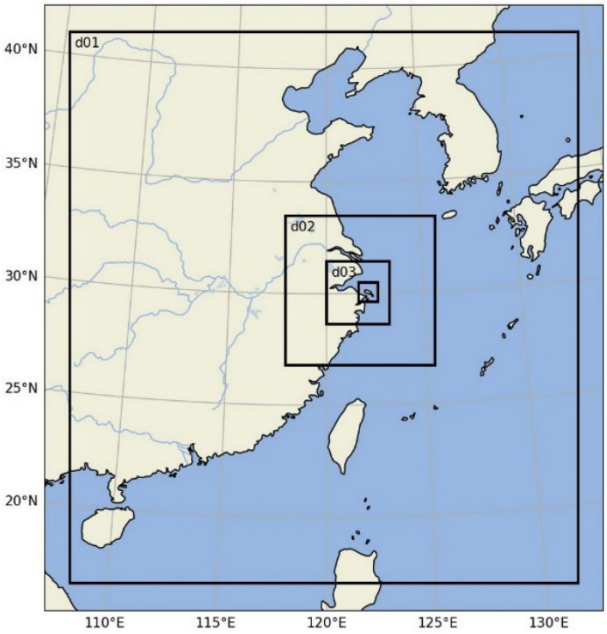

Figure 4. Nested domains from d01 to d04.

Table 1. Spatial and temporal resolutions of WRF domains.

Nested domain	Mesh size (m)	Horizontal scale (km)	Time step (s)
d01	12000	211×229	60
d02	4000	187×172	20
d03	1333.3	235×193	6.67
d04	444.4	220×178	2.22

Table 2. Parameterizations of physical processes.

Model parameter	Description
Dynamics	Advanced Research WRF
Simulation period	2019 Aug. 07-Aug. 13
Microphysics	WRF Double-Moment 6-class
Radiation	Dudhia scheme and RRTM scheme
Land-surface	Unified Noah LSM
Surface layer	Revised MM5 Monin–Obukhov similarity scheme
PBL scheme	YSU
Ocean model	A simple OML model
Air-sea frictional formulation	Donelan scheme

3.2. Simulated Tracks and Intensity

Figure. 5 shows the result of the simulated track and CMA best track records [41,42] (https://tcdata.typhoon.org.cn). As we can see, the ARW model fully reproduces the movement

 doi:10.20944/preprints202404.0999.v1

trajectory of the typhoon's first landfall, reentry into the sea, and subsequent landfall and the simulated track closely matches the observation. Figure. 6 presents the time series of the minimum sea level pressure (SLP) and the maximum sustained wind (MSW) velocity derived from simulation and CMA observation. Before making landfall in Zhejiang, the simulation underestimates the intensity of Lekima with lower MSW and higher minimum SLP, while the intensity results are in good agreement with observations after landfall.

Figure 5. Simulated track of Lekima (red) and CMA best track dataset (black).

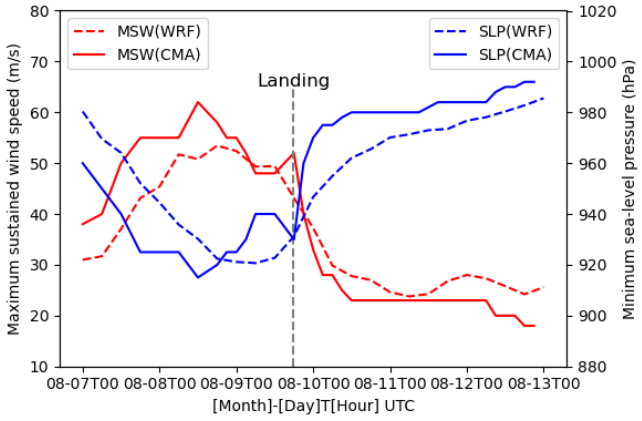

Figure 6. Maximum sustained wind speed and minimum sea-level pressure of Lekima.

3.3. Simulated Wind Field and Precipitation

The evolution of typhoon wind field from 0000 UTC 09 Aug to 0060 UTC 10 Aug 2019 at 30m above the ground level in WRF d02 domain is plotted with a time interval of 6 hours in Figure 7 (Zhoushan island is marked with a red dot). It shows that the ARW model successfully captured the process of Lekima gradually approaching Zhejiang and reducing its intensity immediately when reaching the coastal area before making landfall due to the mechanical dragging. During this process, the local wind velocity in Zhoushan island was greatly influenced by the mesoscale spiral structure of Lekima. Figure 7 marks the location of six ground meteorological stations near the east coast of China and Figure 8 compares the simulated 6-h averaged rainfall intensity at these stations with the observation data obtained from China Meteorological Data Service Centre (https://data.cma.cn/). It shows that extreme heavy rainfall occurs from 0000 UTC 09 Aug to 1200 UTC 10 Aug and the ARW

Preprints.org (www.preprints.org) | NOT PEER-REVIEWED | Posted: 16 April 2024 doi:10.20944/preprints202404.0999.v1

model reproduced the rainfall event successfully. The simulated rainfall intensity at coastal stations (Shangyu, Hongjia and Yuhuan) match the observation more closely, compared to the inland areas (Huzhou, Linan, Hangzhou), because the complex surface condition increases the uncertainty of precipitation simulation. The simulated results indicate that the proposed WRF method could regenerate the whole process of typhoon events and reproduce the strong wind fields and local extreme heavy rainfall with a reasonable accuracy.

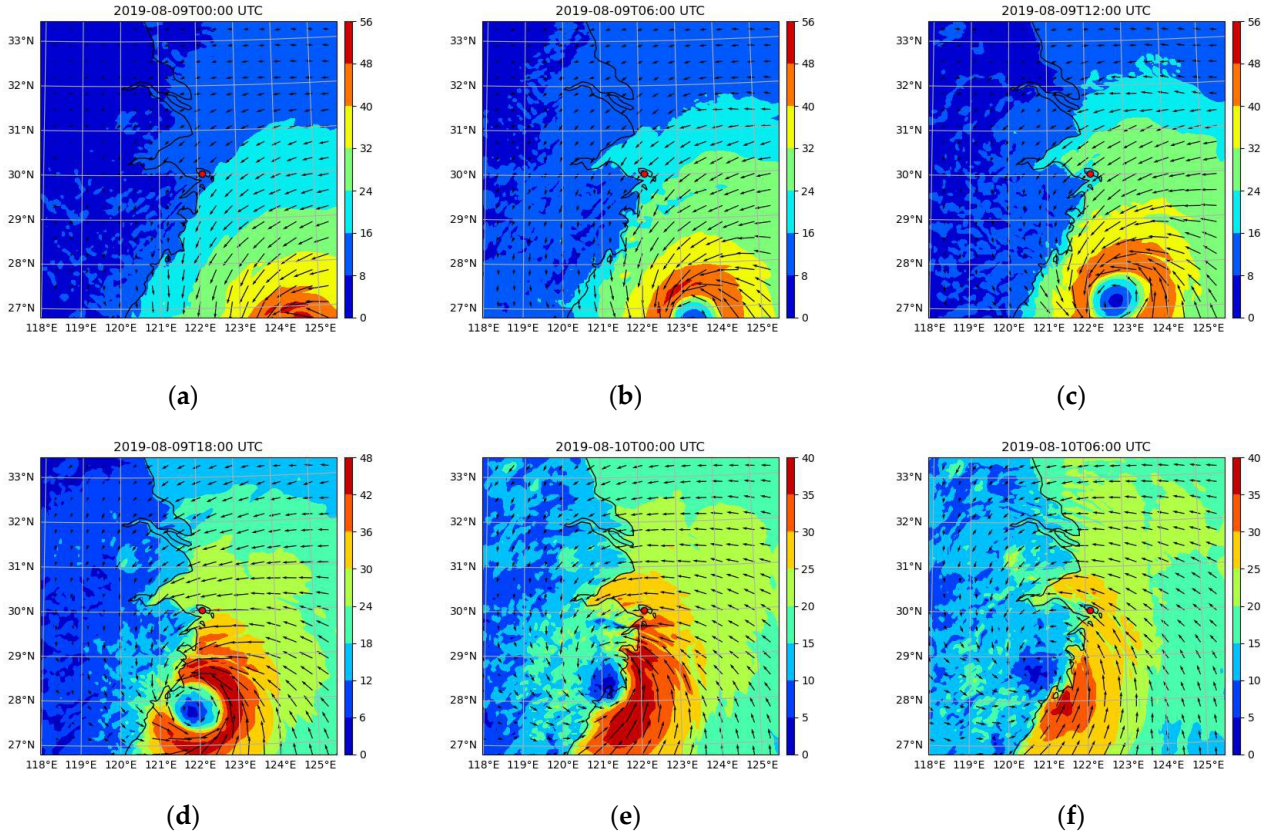

Figure 7. Simulated wind field at 30m above the ground level in WRF d02 domain.

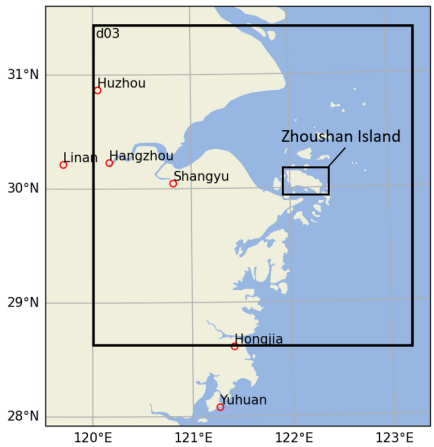

Figure 8. Location of six meteorological stations in Zhejiang province.

Preprints.org (www.preprints.org) | NOT PEER-REVIEWED | Posted: 16 April 2024 doi:10.20944/preprints202404.0999.v1

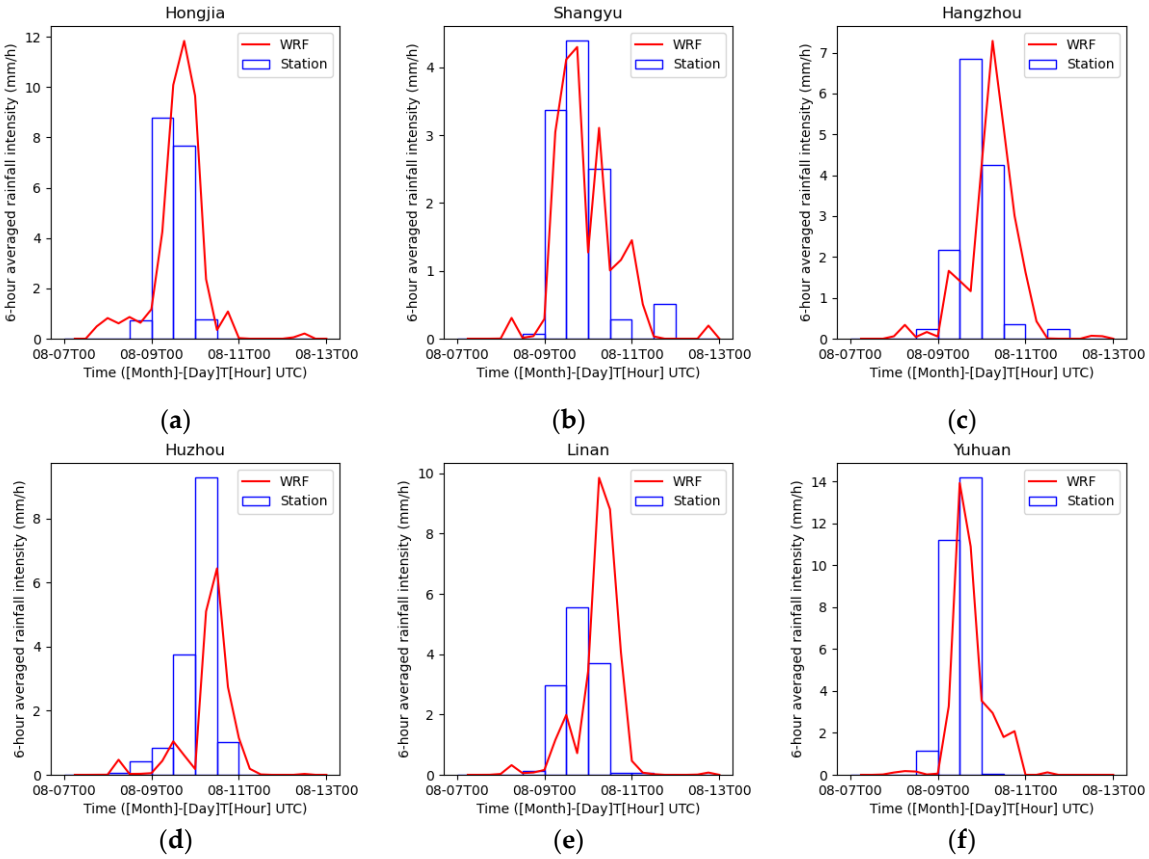

Figure 9. 6-hour averaged rainfall intensity at six meteorological stations during Lekima.

4. Wind-Driven Rain Load on Conductor

After the mesoscale WRF simulation of Lekima, local wind field and rainfall intensity in Zhoushan island is obtained, and the subsequent procedure of our simulation system is to solve the coupled wind and rain field around the transmission line and find out the WDR load on conductors. The WDR simulation would be carried out on 0000 UTC 10 Aug with the mean wind speed of $U = 20.3$ m/s, the wind angle of $\beta = 12.1^{\circ}$ and the rainfall intensity of $R_{\mathrm{h}} = 39$ mm/h for the targeted transmission line in Zhoushan island as shown in Figure 10. Two-dimensional computational domains and meshes of the fluid region around the cross-section of the conductor are established as presented in Figure 11. Based on the drag coupling between rain phases and wind phase, the horizontal raindrop velocities are assumed to be equal to the inflow wind velocity, and the vertical velocities of rain phases are set by Eq. (10). The phase volume fraction α_k at the inlet boundary can be calculated as,

$$\alpha_k = \frac{R_{\mathrm{h}} f_{\mathrm{h}}\left(R_{\mathrm{h}}, D\right)}{V_{\mathrm{t}}\left(D\right)}, \tag{19}$$

where R_{h} is the rainfall intensity; $f_{\mathrm{h}}\left(R_{\mathrm{h}}, D\right)$ represents the volume fraction of raindrops with diameter D in all raindrops passing through a unit area horizontal plane in unit time, i.e., flux fraction, can be calculated as,

$$f_{\mathrm{h}}\left(R_{\mathrm{h}}, D\right) = \frac{D^3 N\left(R_{\mathrm{h}}, D\right) V_{\mathrm{t}}\left(D\right)}{\int_0^{\infty} D^3 N\left(R_{\mathrm{h}}, D\right) V_{\mathrm{t}}\left(D\right) dD}, \tag{20}$$

where $N\left(R_{\mathrm{h}}, D\right)$ is the raindrop size distribution function which follows the modified Λ distribution proposed by de Wolf [40], and is expressed as,

 doi:10.20944/preprints202404.0999.v1

$$N\left(R_{\mathrm{h}},D\right)=N_0\left(R_{\mathrm{h}}\right)D^{2.93}\exp\left(-\Lambda\left(R_{\mathrm{h}}\right)D\right), \tag{21}$$

$$N_0\left(R_{\mathrm{h}}\right)=1.98\times10^{-5}R_{\mathrm{h}}^{-0.384} \tag{22}$$

$$\Lambda\left(R_{\mathrm{h}}\right)=5.38R_{\mathrm{h}}^{-0.186} \tag{23}$$

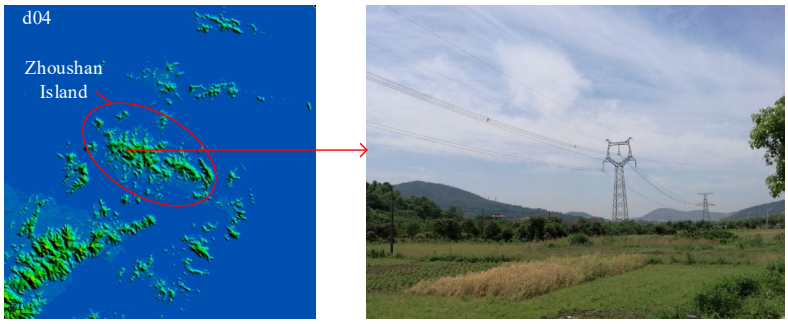

Figure 10. Location of the target transmission line.

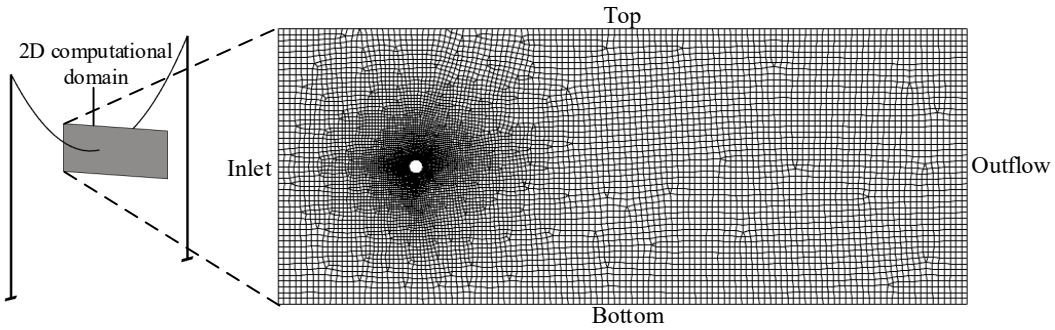

Figure 11. 2D mesh of computational domain for WDR.

Figure 12 presents the rain phase flux fraction with different rainfall intensities. According to the illustrated raindrop size distribution, the discretized raindrop sizes are set to be $D=0.5\sim6.0$ mm with the increment $\Delta D=0.5$ mm as inlet rain condition, for the WDR simulation of rainfall intensity $R_{\mathrm{h}}=39$ mm/h .

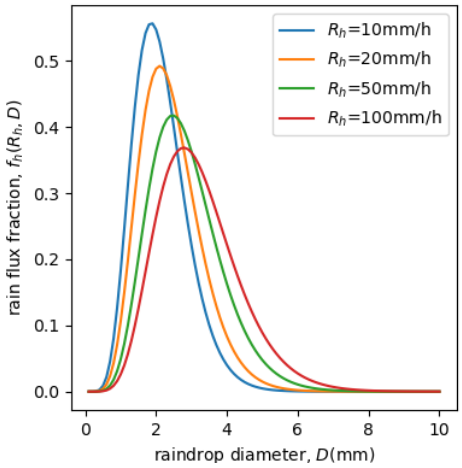

Figure 12. Fraction of rain flux corresponding to raindrop with diameter *d*.

Preprints.org (www.preprints.org) | NOT PEER-REVIEWED | Posted: 16 April 2024 doi:10.20944/preprints202404.0999.v1

The volume fraction and raindrop velocities at the top boundary are defined in the same way as the inlet boundary condition. The boundary conditions at the bottom, outflow boundary and the conductor surface are defined as,

$$\begin{cases} \dfrac{\partial \alpha_k}{\partial \boldsymbol{n}} = 0, & \dfrac{\partial \boldsymbol{u}_k}{\partial \boldsymbol{n}} = 0 \quad \text{for } \boldsymbol{u}_k \cdot \boldsymbol{n} > 0 \\ \alpha_k = 0, & \boldsymbol{u}_k = 0 \quad \text{for } \boldsymbol{u}_k \cdot \boldsymbol{n} < 0 \end{cases}, \tag{24}$$

where $\boldsymbol{n}$ is the unit normal vector pointing out of the computational domain. The first expression in Eq. (24) indicates that the raindrops will impact the solid surface just like no blocking. Therefore, based on the momentum theorem, the rain load caused by raindrop impact can be calculated as [44],

$$p_{rain} = \int_0^\infty \rho_l \alpha_k V_n(D_k)^2 dD_k \,, \tag{25}$$

$$\tau_{rain} = \int_0^\infty \rho_l \alpha_k V_n(D_k) V_\tau(D_k) dD_k \tag{26}$$

where p_{rain} and τ_{rain} refers to the rain phase pressure produced by the momentum loss in the normal and tangential direction, respectively. $V_n(D_k)$ and $V_\tau(D_k)$ are the velocity of rain phase with diameter D_k towards the solid surface along normal and tangential direction, respectively. Then the C_{drag} and C_{lift} under WDR condition can be derived from the summation of wind pressure and rain phase pressure as,

$$C_{drag} = \frac{\oint (p_{\text{rain}} + p_{\text{wind}}) dA_z + (\tau_{\text{rain}} + \tau_{\text{wind}}) dA_y}{\frac{1}{2} \rho_a U_0^2 d}, \tag{27}$$

$$C_{lift} = \frac{\oint (p_{\text{rain}} + p_{\text{wind}}) dA_y + (\tau_{\text{rain}} + \tau_{\text{wind}}) dA_z}{\frac{1}{2} \rho_a U_0^2 d} \tag{28}$$

Figure 13 shows the simulated drag and lift coefficients of the conductor with upper rivulet under coupled wind and rain condition. Compared to cases without rain, both the drag and lift coefficients exhibit obvious variation from the constant results without rain. The result shows that the derivative of drag coefficients with respect to angle suddenly changed from negative to positive, and the derivative of lift coefficients changed from positive to negative when the attack angle $\lambda \approx 39^\circ$, which is the critical angle causing boundary layer to trip and influencing the location of the separation point [14].

 doi:10.20944/preprints202404.0999.v1

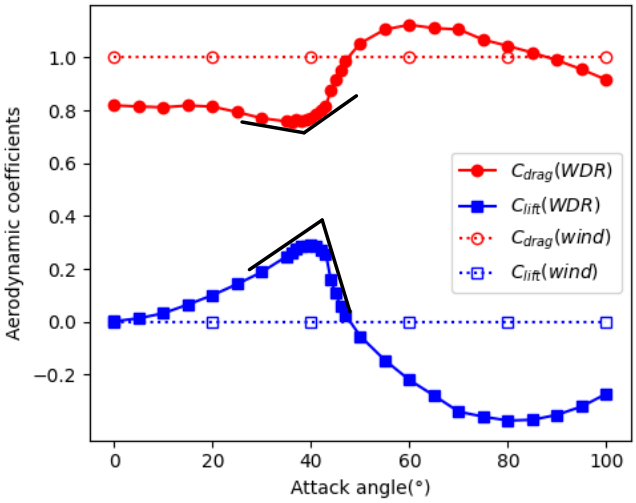

Figure 13. Aerodynamic coefficients of conductor cross-section with wind-driven rain effect.

5. Motion of Conductor under WDR

The transmission line in Zhoushan island consists of two spans of 160 m and 260 m. Each sub-conductor of the quad-bundled conductor is made of JL/G1A-300/25, the physical parameters of which are listed in Table 3. In the table, A_c is the calculated cross-sectional area of the conductor; D_c is the outer diameter; ρ_L is the mass per unit length; E is the elastic modulus; T_Y is the tensile strength of the conductor. To improve computational efficiency, the four sub-conductors of the quad-bundled conductor are modelled as a single equivalent conductor. The cross-sectional area, mass per unit length, and other physical parameters are adjusted accordingly for the single equivalent conductor to create a simplified two-span transmission line model, as shown in Figure 14.

Table 3. Physical parameters of single conductor (JL/G1A-300/25).

A_c(mm^2)	D_c(mm)	ρ_L(kg·m^{-1})	E(GPa)	T_Y(kN)
333.31	23.8	1.057	65	83.76

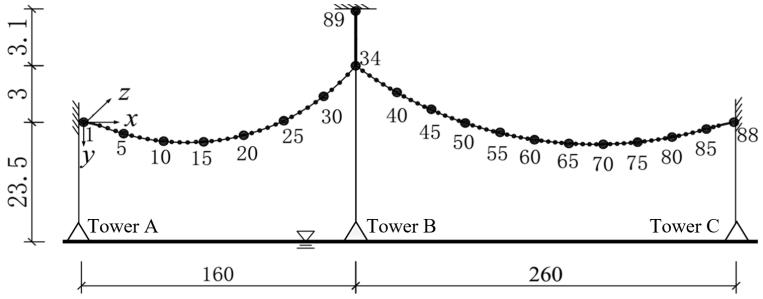

Figure 14. Finite element model of the overhead conductor. (Length unit: m).

For applying wind or WDR loads, total 89 loading nodes are defined along the transmission line in Figure 14. The mean wind velocity and rainfall intensity affecting the transmission line during Lekima in terms of WDR loads are derived from the WDR simulation as presented in Section 4. Local turbulence wind fields are numerically generated by the spectral representation method [45]. Figure 15 shows the generated fluctuating wind velocity at node 34.

 doi:10.20944/preprints202404.0999.v1

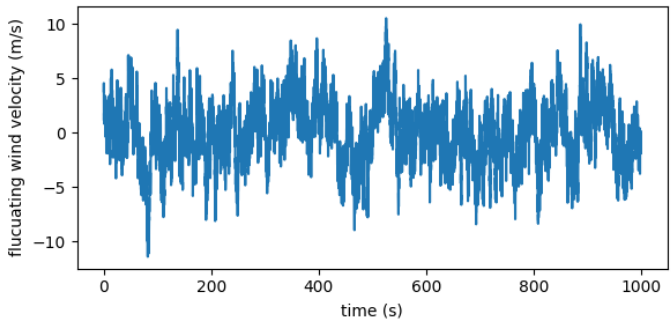

Figure 15. Generated turbulent wind velocity at node 34.

According with the derived wind-driven rain meteorological condition and the aerodynamic force coefficients presented in Figure 13, the wind-driven rain loads are applied to the finite element model of the transmission line, and dynamic response analysis of the transmission line is carried out. The initial geometric configuration of the conductor under gravity can be precisely described using the catenary equation, which could be approximated by the parabolic equation for a small ratio of sag to span, i.e., less than 1/8. Figure 16 compares the displacements of node 34 subjected to wind loads and WDR loads. The result shows that the WDR loads would produce more significant horizontal displacements than those by wind loads only. The greater WDR load effects could be attributed to the occurrence of the upper rivulet and the impingement of raindrops. Figure 17 presents the mean and standard deviation of horizontal displacements along the transmission line with node number. It is found that the standard deviation of horizontal displacement shows little difference between two cases of wind loads and WDR loads, while the mean values under the WDR loads are significantly greater than those of wind loads with increase rates around 17%~18%. Such larger swing behavior of the overhead conductor due to WDR loads indicates that it is necessary to take account into the WDR loads in the design of transmission lines for extreme weather conditions of typhoons.

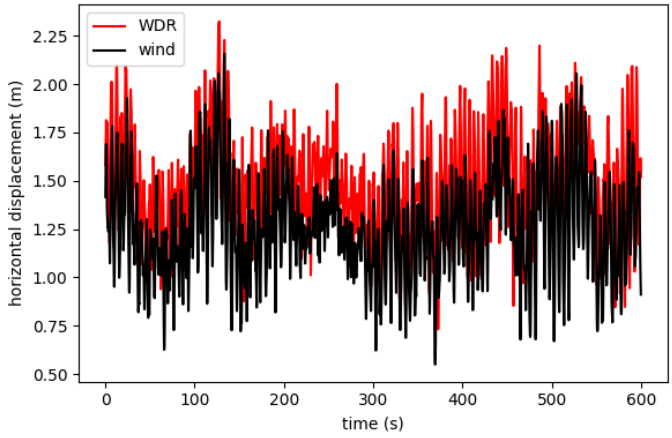

Figure 16. Horizontal displacements of node 34 under WDR and wind load.

 doi:10.20944/preprints202404.0999.v1

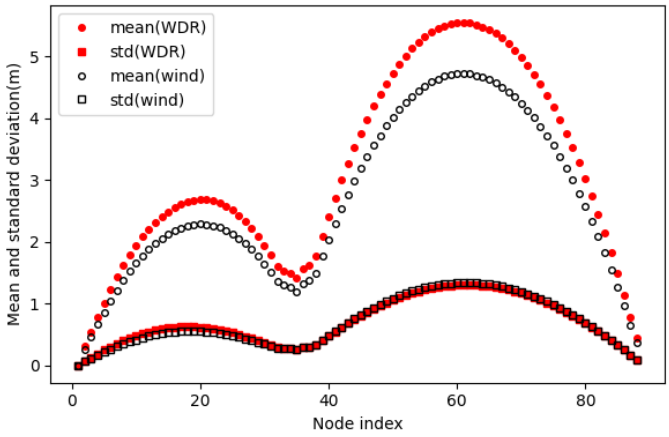

Figure 17. Mean and standard deviation of horizontal displacements.

6. Discussion and Conclusions

In this paper, a multi-scale WRF-CFD-FEM numerical framework is developed to analyze the motions of the transmission line subjected to coupled wind and rain loads during typhoon events. A case study was presented in detail by solving the dynamic responses of a full-scale transmission line located in Zhoushan island during Super Typhoon Lekima (2019). The proposed framework firstly reproduced the evolution of super typhoon Lekima, including the wind field and precipitation distribution at the coastal area using mesoscale weather model WRF. Then the coupled wind and rain fields around the transmission line were simulated by the Eulerian multiphase CFD model. Finally, the motion of the conductor under joint actions of wind and rain, i.e., WDR loads, were solved by the finite element method. Some conclusions are summarized as follows:

(1) The ARW model is capable of simulating the track and intensity evolution of typhoon events. It can also explicitly resolve the typhoon wind field and the associated precipitation for a target region. The simulated wind and rain results of Super Typhoon Lekima show good agreements with observations.

(2) The coupled effect of wind and rain load consists of the upper rivulet attached to the conductor surface and the direct impingement of raindrops. The simulated drag and lift coefficients of the overhead conductor under WDR conditions exhibit noticeable variations with the wind angle of attack.

(3) The proposed multiscale WRF-CFD-FEM numerical framework could be used to analyze and predict the dynamic responses of transmission lines under typhoon conditions by considering coupled wind and rain effects. In the case study of Super Typhoon Lekima, the horizontal displacements of the transmission line under the coupling of wind and rain are significantly larger than those of wind loads only. The increasing rates of 17%~18% were found for the mean displacements under WDR loads compared to the wind loads. Such larger swing behavior of the overhead conductor due to WDR loads indicates the importance of coupled effects of wind and rain during typhoon conditions for the design of transmission lines.

Funding: Supports for this research are provided by Ningbo Key R&D Program (Project No. 2023Z221), National Natural Science Foundation of China (Project No. 52178512) and Natural Science Foundation of Zhejiang Province (Project No. LZ22E080006).

Conflicts of Interest: The authors declare no conflict of interest.

References

1. Fang, Z., Wang, Z., Zhu, R. & Huang, H. Study on Wind-Induced Response of Transmission Tower-Line System under Downburst Wind. *Buildings* **12**, 891 (2022).

 doi:10.20944/preprints202404.0999.v1

2. Wang, Z. & Wang, Z. A novel preventive islanding scheme of power system under extreme typhoon events. *International Journal of Electrical Power & Energy Systems* **147**, 108857 (2023).
3. Jeddi, A. B. *et al.* Multi-hazard typhoon and earthquake collapse fragility models for transmission towers: An active learning reliability approach using gradient boosting classifiers. *Earthquake Engineering & Structural Dynamics* **51**, 3552–3573 (2022).
4. Guan, R., Xiang, C. & Jia, Z. Anti-Wind Experiments and Damage Prediction of Transmission Tower under Typhoon Conditions in Coastal Areas. *Energies* **15**, 3372 (2022).
5. Lange, S. *et al.* Projecting Exposure to Extreme Climate Impact Events Across Six Event Categories and Three Spatial Scales. *Earth's Future* **8**, e2020EF001616 (2020).
6. Huang, M. *et al.* Increasing typhoon impact and economic losses due to anthropogenic warming in Southeast China. *Sci Rep* **12**, 14048 (2022).
7. van der Burgh, A. H. P. & Hartono. Rain-wind-induced vibrations of a simple oscillator. *International Journal of Non-Linear Mechanics* **39**, 93–100 (2004).
8. van der Burgh, A. H. P., Hartono & Abramian, A. K. A new model for the study of rain-wind-induced vibrations of a simple oscillator. *International Journal of Non-Linear Mechanics* **41**, 345–358 (2006).
9. Deng, H. Z., Xu, H. J., Duan, C. Y., Jin, X. H. & Wang, Z. H. Experimental and numerical study on the responses of a transmission tower to skew incident winds. *Journal of Wind Engineering and Industrial Aerodynamics* **157**, 171–188 (2016).
10. Yang, S. C. & Hong, H. P. Nonlinear inelastic responses of transmission tower-line system under downburst wind. *Engineering Structures* **123**, 490–500 (2016).
11. An, L., Guan, Y., Zhu, Z., Wu, J. & Zhang, R. Structural failure analysis of a river-crossing transmission line impacted by the super typhoon Rammasun. *Engineering Failure Analysis* **104**, 911–931 (2019).
12. An, L., Wu, J., Zhang, Z. & Zhang, R. Failure analysis of a lattice transmission tower collapse due to the super typhoon Rammasun in July 2014 in Hainan Province, China. *Journal of Wind Engineering and Industrial Aerodynamics* **182**, 295–307 (2018).
13. Yan, B., Lin, X., Luo, W., Chen, Z. & Liu, Z. Numerical Study on Dynamic Swing of Suspension Insulator String in Overhead Transmission Line under Wind Load. *IEEE Transactions on Power Delivery* **25**, 248–259 (2010).
14. Zhou, C., Yin, J. & Liu, Y. Large Swing Behavior of Overhead Transmission Lines under Rain-Load Conditions. *Energies* **11**, 1092 (2018).
15. Fu, X. & Li, H.-N. Dynamic analysis of transmission tower-line system subjected to wind and rain loads. *Journal of Wind Engineering and Industrial Aerodynamics* **157**, 95–103 (2016).
16. Fu, X. & Li, H.-N. Effect of Raindrop Size Distribution on Rain Load and Its Mechanism in Analysis of Transmission Towers. *International Journal of Structural Stability and Dynamics* **18**, 1850115 (2018).
17. Zhou, C., Liu, Y. & Ma, Z. Investigation on aerodynamic instability of high-voltage transmission lines under rain-wind condition. *J Mech Sci Technol* **29**, 131–139 (2015).
18. Zhou, C., Yin, J. & Liu, Y. Effects of wind and rain on the motion of the high-voltage conductor in a simplified valley terrain. *Electric Power Systems Research* **173**, 153–163 (2019).
19. Bauer, P., Thorpe, A. & Brunet, G. The quiet revolution of numerical weather prediction. *Nature* **525**, 47–55 (2015).
20. Yeh, K.-S. *et al.* Performance of the experimental HWRF in the 2008 Hurricane Season. *Nat Hazards* **63**, 1439–1449 (2012).
21. Huang, M., Wang, Y., Lou, W. & Cao, S. Multi-scale simulation of time-varying wind fields for Hangzhou Jiubao Bridge during Typhoon Chan-hom. *Journal of Wind Engineering and Industrial Aerodynamics* **179**, 419–437 (2018).
22. Xu, H. *et al.* Indirect Effects of Binary Typhoons on an Extreme Rainfall Event in Henan Province, China From 19 to 21 July 2021. 3. Sensitivities to Microphysics Schemes. *Journal of Geophysical Research: Atmospheres* **128**, e2022JD037936 (2023).
23. Park, J. *et al.* Sensitivity of Real-Time Forecast for Typhoons Around Korea to Cumulus and Cloud Microphysics Schemes. *Journal of Geophysical Research: Atmospheres* **128**, e2022JD036709 (2023).
24. Wang, M., Zhao, K., Pan, Y. & Xue, M. Evaluation of Simulated Drop Size Distributions and Microphysical Processes Using Polarimetric Radar Observations for Landfalling Typhoon Matmo (2014). *Journal of Geophysical Research: Atmospheres* **125**, e2019JD031527 (2020).

 doi:10.20944/preprints202404.0999.v1

25. Blocken, B. & Carmeliet, J. A review of wind-driven rain research in building science. *Journal of Wind Engineering and Industrial Aerodynamics* **92**, 1079–1130 (2004).
26. Ge, H., Deb Nath, U. K. & Chiu, V. Field measurements of wind-driven rain on mid-and high-rise buildings in three Canadian regions. *Building and Environment* **116**, 228–245 (2017).
27. Kubilay, A., Derome, D., Blocken, B. & Carmeliet, J. High-resolution field measurements of wind-driven rain on an array of low-rise cubic buildings. *Building and Environment* **78**, 1–13 (2014).
28. Blocken, B., Dezsö, G., van Beeck, J. & Carmeliet, J. Comparison of calculation models for wind-driven rain deposition on building facades. *Atmospheric Environment* **44**, 1714–1725 (2010).
29. Ge, H., Chiu, V., Stathopoulos, T. & Souri, F. Improved assessment of wind-driven rain on building façade based on ISO standard with high-resolution on-site weather data. *Journal of Wind Engineering and Industrial Aerodynamics* **176**, 183–196 (2018).
30. Huang, S. H. & Li, Q. S. Numerical simulations of wind-driven rain on building envelopes based on Eulerian multiphase model. *Journal of Wind Engineering and Industrial Aerodynamics* **98**, 843–857 (2010).
31. Kubilay, A., Derome, D., Blocken, B. & Carmeliet, J. Numerical simulations of wind-driven rain on an array of low-rise cubic buildings and validation by field measurements. *Building and Environment* **81**, 283–295 (2014).
32. Wang, X. J., Li, Q. S. & Li, J. C. Field measurements and numerical simulations of wind-driven rain on a low-rise building during typhoons. *Journal of Wind Engineering and Industrial Aerodynamics* **204**, 104274 (2020).
33. Kubilay, A., Derome, D., Blocken, B. & Carmeliet, J. CFD simulation and validation of wind-driven rain on a building facade with an Eulerian multiphase model. *Building and Environment* **61**, 69–81 (2013).
34. Kubilay, A., Derome, D., Blocken, B. & Carmeliet, J. Wind-driven rain on two parallel wide buildings: Field measurements and CFD simulations. *Journal of Wind Engineering and Industrial Aerodynamics* **146**, 11–28 (2015).
35. Skamarock, W. C. & Klemp, J. B. A time-split nonhydrostatic atmospheric model for weather research and forecasting applications. *Journal of Computational Physics* **227**, 3465–3485 (2008).
36. Laprise, R. The Euler Equations of Motion with Hydrostatic Pressure as an Independent Variable. *Monthly Weather Review* **120**, 197–207 (1992).
37. Lim, K.-S. S. & Hong, S.-Y. Development of an Effective Double-Moment Cloud Microphysics Scheme with Prognostic Cloud Condensation Nuclei (CCN) for Weather and Climate Models. *Monthly Weather Review* **138**, 1587–1612 (2010).
38. Locatelli, J. D. & Hobbs, P. V. Fall speeds and masses of solid precipitation particles. *Journal of Geophysical Research (1896-1977)* **79**, 2185–2197 (1974).
39. Mätzler, C. Drop-Size Distributions and Mie Computations for Rain. *Bern, Switzerland: Institute of Applied Physics, University of Bern* (2002).
40. Hikami, Y. & Shiraishi, N. Rain-wind induced vibrations of cables stayed bridges. *Journal of Wind Engineering and Industrial Aerodynamics* **29**, 409–418 (1988).
41. Ying, M. et al. An Overview of the China Meteorological Administration Tropical Cyclone Database. Journal of Atmospheric and Oceanic Technology 31, 287–301 (2014).
42. Lu, X. et al. Western North Pacific Tropical Cyclone Database Created by the China Meteorological Administration. Adv. Atmos. Sci. 38, 690–699 (2021).
43. de Wolf, D. A. On the Laws-Parsons distribution of raindrop sizes. *Radio Science* **36**, 639–642 (2001).
44. Huang, S., Li, Q., Liu, M., Chen, F. & Liu, S. Numerical Simulation of Wind-Driven Rain on a Long-Span Bridge. *Int. J. Str. Stab. Dyn.* **19**, 1950149 (2019).
45. Shinozuka, M. & Deodatis, G. Simulation of Stochastic Processes by Spectral Representation. *Applied Mechanics Reviews* **44**, 191–204 (1991).